Renewable Energy and Power Quality Journal
https://repqj.com/index.php/repqj/index
RE&PQJ, Vol. 24, No. 3, 2026

Data-Driven Governing Equations for Agricultural Biomass-CoalCo-Pyrolysis: SINDy Kinetics, Flory-Huggins Synergy, and High-Performance Char

K. H. Arunkumar[1,*], Krantikumar Kshaurad[2]

[1]Department of Mechanical Engineering, CMR University, Bengaluru 562149, Karnataka, India
ORCID: 0000-0002-7971-0501

[2]Department of Mechanical Engineering, Dayananda Sagar College of Engineering, Bengaluru 560078, Karnataka, India
ORCID: 0000-0001-9911-5083

[*]Corresponding author: K. H. Arunkumar, arun.k@cmr.edu.in

Article History

Received: 07 May 2026 Revised: 30 June 2026 Accepted: 01 July 2026 Available Online: 14 July 2026

Abstract. Agricultural biomass co-pyrolysis with coal offers a near-term strategy for biomass valorisation and fossil carbon displacement, yet the mechanistic basis for the consistently observed equimolar blend optimum has remained unexplained. This study applies five interconnected mathematical layers — sparse governing equation discovery (SINDy), symbolic regression, transfer entropy analysis, persistent homology, and variational energy landscape formulation — to the co-pyrolysis of three South Asian agricultural residues (rice husk, areca husk, sugarcane husk) with Ramgarh coal at blend fractions of 25, 50, and 75 wt% across heating rates of 10-40 K/min. SINDy recovers a three-term governing differential law without any pre-assumed kinetic model, validated by three independent robustness tests. Symbolic regression identifies a Flory–Huggins configurational entropy origin for co-pyrolysis synergy, outperforming classical additive and Langmuir benchmarks. Persistent homology detects three distinct topological reaction phases and a statistically confirmed synergy loop at the equimolar blend. A variational energy landscape, proven stable by Lyapunov analysis, unifies all prior findings and links the 28.8% barrier reduction to a ~508-fold rate enhancement at 500 K via Transition State Theory. The 50 wt% biomass blend (B50) delivers super-additive BET surface areas, CO_2 uptake, and Pb^{2+} removal across all three biomass systems, with all chars exceeding EPA TCLP safety margins. A minimal 7-measurement protocol recovers full system governing laws, representing a 14-fold compression over standard characterisation effort.

Key words. Co-pyrolysis, SINDy, Agricultural biomass, Synergistic char, CO_2 adsorption, Pb^{2+} remediation, Energy landscape, Circular bioeconomy

1. Introduction

The global energy transition demands near-term strategies for reducing fossil carbon demand without stranding existing thermal infrastructure [1-3]. In South and Southeast Asia, rice husk, areca husk, and sugarcane husk together account for more than 180 million tonnes of annual agricultural residue, the great majority of which is open-burned at field margins — releasing particulate matter, methane, and CO_2 with no energy recovery [2,4]. Co-pyrolysis with coal addresses this on two fronts simultaneously: It valorises the biomass waste stream and partially displaces coal, while yielding a solid char with surface chemistry suited to CO_2 capture and heavy-metal remediation [1,5-7]. The broader context of renewable fuel blending — from biodiesel in compression-ignition engines [8] to biomass-derived pyrolytic oils [9,10] — underscores a consistent principle: Blending renewable and fossil-derived components at optimal ratios consistently outperforms the pure-component expectations.

Biomass–coal co-pyrolysis has attracted sustained experimental and modelling attention over the past decade [1,3-6,11-15]. Liu et al. [14] conducted a recent kinetic study on coal and biomass co-pyrolysis confirming super-additive behaviour at intermediate blend ratios, while Jena et al. [6] provide a comprehensive mechanistic review of co-pyrolysis across diverse feedstock combinations. Analytical methods for thermochemical characterisation — including TG-FTIR [11] and advanced spectroscopic approaches [16] — have documented synergistic product distributions, yet the fundamental governing differential equation of the process has never been directly identified from data. Machine learning has been applied to co-

pyrolysis performance prediction [12,15], and recent SHAP-based analysis [15] provides variable importance rankings, but these approaches remain predictive rather than explanatory: They cannot identify why the equimolar blend is consistently optimal. Deng et al. [7] and Lv et al. [9] further demonstrate that co-pyrolysis chars from diverse feedstream combinations exhibit broadly useful environmental remediation properties, but again without a mechanistic explanation for the observed optima. The gap in the field is specific: No study has recovered the governing kinetic differential equation from data, identified its functional form as a Flory-Huggins configurational entropy expression, or provided a variational energy landscape that unifies these findings.

This paper closes that gap by applying five interconnected mathematical layers: (I) sparse governing equation discovery via SINDy [17-20]; (II) symbolic regression by genetic programming [21,22]; (III) information-theoretic directed dependency analysis [23]; (IV) topological phase characterisation by persistent homology [24-27]; and (V) a variational energy landscape formulation [28-30]. The energy landscape (Layer V) provides the primary theoretical contribution: A rigorous variational foundation that proves Lyapunov stability for three reaction basins and connects the SINDy-discovered barrier structure to Transition State Theory rate predictions [28]. The five layers are not independent analyses; each answers a question the preceding layer cannot, and together they produce a unified, mechanistically grounded account of co-pyrolysis synergy. The key novel contributions are: (i) first application of SINDy to co-pyrolysis kinetics recovering the governing law without model assumption [17]; (ii) identification of the Flory-Huggins form $\Delta E\alpha \propto \varphi(1-\varphi)$ by genetic programming [21,31]; (iii) topological confirmation of a $\beta_1 = 1$ synergy loop at B50 by persistent homology [24,27]; (iv) variational energy landscape with Lyapunov stability proof; and (v) a validated minimal-data protocol (seven measurements, 14× compression) for full system characterisation. The experimental system comprises rice husk (RH), areca husk (AH), and sugarcane husk (SH) blended with Ramgarh coal (RC) at blend fractions of 25, 50, and 75 wt%, with functional char performance evaluated for CO_2 capture and Pb^{2+} remediation.

2. Materials and Experimental Methods

2.1 Feedstocks and Blend Preparation

Rice husk (RH), areca nut husk (AH), and sugarcane husk (SH) were sourced from registered agricultural processing cooperatives in Tumkur district, Karnataka, India (supplier registration Nos. KSUPP-2024-RH-041, AH-038, SH-056). Ramgarh coal (RC) — a sub-bituminous coal from the Ramgarh Colliery, Jharkhand, India — was procured from a BIS-certified coal supplier (CIL subsidiary). All materials were dried at 105°C for 24 h in a convection oven prior to size reduction.

Grinding and sieving: All feedstocks were jaw-crushed, then sieved to a particle size fraction of 150-250 μm (ASTM No. 60-70 mesh). Particle size was confirmed by laser diffraction (Malvern Mastersizer 3000; d_{50} = 195 μm for all materials). Blend homogenisation: Binary blends were prepared at biomass: Coal mass fractions of 25:75 (B25), 50:50 (B50), and 75:25 (B75). Weighed portions were combined in a sealed rotary mixer (IKA TUBE 2000, 30 rpm, 30 min) to ensure thorough mechanical intermixing. Blend homogeneity was verified by running three independent TGA replicates per blend; the coefficient of variation (CV) of DTG peak temperature across replicates was below 1.5°C for all 13 sample types, confirming adequate blend uniformity. Blend designations: RH-B25, RH-B50, RH-B75; AH-B25, AH-B50, AH-B75; SH-B25, SH-B50, SH-B75; plus pure RH, AH, SH, and RC (13 sample types total).

2.2 Proximate and Elemental Characterisation

Proximate analysis followed ASTM D3172/D3175/D3174. Higher heating value (HHV) was measured by bomb calorimetry (IKA C6000; calibrated against certified benzoic acid; CV ≤ 0.15%). Ultimate analysis was performed by CHNS combustion (Elementar Vario EL Cube). Ash oxide composition was determined by WDXRF (Rigaku ZSX Primus IV) on samples ashed at 815°C. ICP-OES (Thermo Fisher iCAP 7400) quantified trace metals after microwave-assisted aqua regia digestion. All values are mean ± SD from six replicates on an air-dry basis. Table 1 summarises proximate and HHV data for selected samples.

Table 1. Proximate analysis and HHV for key samples (ASTM D3172; n = 6, air-dry basis).

Sample	Type	Moisture (%)	VM (%)	FC (%)	Ash (%)	HHV (MJ/kg)
RH	Biomass	8.43±0.19	62.27±0.53	16.61±0.34	12.69±0.26	15.14±0.17
AH	Biomass	9.28±0.22	68.31±0.57	14.23±0.31	8.18±0.20	16.79±0.18
SH	Biomass	7.86±0.17	71.14±0.61	13.68±0.29	7.32±0.19	17.83±0.16
RC	Coal	5.14±0.16	28.47±0.41	48.31±0.47	18.08±0.33	24.13±0.22
RH–B50	Blend	6.92±0.18	45.68±0.48	32.24±0.43	15.16±0.28	19.61±0.20
AH–B50	Blend	7.31±0.19	48.64±0.49	31.07±0.44	12.98±0.27	20.47±0.20
SH–B50	Blend	6.57±0.17	49.81±0.50	31.12±0.44	12.50±0.26	20.93±0.20

2.3 Thermogravimetric Analysis

TGA was performed on a TA Instruments SDT Q600. Samples (8-10 mg) in alumina crucibles were heated from ambient to 900°C under nitrogen (50 mL/min) at four heating rates (β = 10, 20, 30, 40 K/min). Temperature calibration used indium (156.60°C) and zinc (419.53°C) melting points. Each sample-heating rate

combination was run in triplicate (n = 3). Mass-loss conversion was calculated as $\alpha(T) = (m_0 - m(T))/(m_0 - m_\infty)$. TG-FTIR analysis was performed for selected samples using a Bruker Tensor 37 FTIR spectrometer in-line with the TGA [11,16].

2.4 Isoconversional Kinetic Analysis

Three model-free isoconversional methods were applied at 17 conversion points (α = 0.10-0.90, step = 0.05). All three methods share the underlying isoconversional principle: At constant α, the reaction rate depends only on temperature, allowing $E\alpha$ to be determined from the slope of a linearised plot across multiple heating rates. The explicit equations are:

Kissinger-Akahira-Sunose (KAS) [32]:

$$\ln\left(\beta_i / T^2_\{\alpha,i\}\right) = \ln\left[AR/\left(E\alpha\, g(\alpha)\right)\right] - E\alpha/RT_\{\alpha,i\} \quad (1)$$

where β_i is the i -th heating rate, $T_\{\alpha,i\}$ is the temperature at conversion α under heating rate β_i, A is the pre-exponential factor, $g(\alpha)$ is the integrated conversion function, and R is the universal gas constant. $E\alpha$ is obtained from the slope $-E\alpha/R$ of a plot of $\ln(\beta/T^2)$ vs. $1/T$ at constant α.

Flynn-Wall-Ozawa (OFW) [33]:

$$\log(\beta_i) = \log\left[AE\alpha/Rg(\alpha)\right] - 2.315 - 0.4567\, E\alpha/RT_\{\alpha,i\} \quad (2)$$

$E\alpha$ is obtained from the slope $-0.4567E\alpha/R$ of $\log(\beta)$ vs. $1/T$.

Starink method [34]:

$$\ln\left(\beta_i / T\text{^}\ \{1.92\}_\{\alpha,i\}\right) = C_S - 1.0008E\alpha/\left(RT_\{\alpha,i\}\right) \quad (3)$$

where C_S is a constant. $E\alpha$ is obtained from the slope $-1.0008E\alpha/R$. Across all 13 samples and three methods, R^2 ranged from 0.914 to 0.998. Maximum method divergence at any single α was less than 8 kJ/mol, confirming method independence. The KAS-derived $E\alpha(\alpha)$ dataset was used as primary SINDy input; method-averaged $E\alpha$ values were used for symbolic regression and energy landscape construction. The full isoconversional dataset comprises 13 samples × 17 conversion points = 221 activation energy-conversion pairs. After central finite-difference derivative computation (excluding the two endpoints), the SINDy library matrix contains N = 195 rows [17].

2.5 BET Porosity and Functional Performance

Nitrogen adsorption-desorption isotherms were measured at 77 K (Micromeritics ASAP 2020). BET surface areas, pore volumes, and micropore fractions were determined at three pyrolysis temperatures (450, 550, 650°C) following IUPAC recommendations [35]. CO_2 adsorption capacity was measured at 273 K and 1 bar by a volumetric method [36]. Pb^{2+} removal was assessed from single-component batch experiments (100 mg/L initial concentration, pH 5.5, 1 g/L char, 24 h, 25°C) with ICP-OES verification. EPA TCLP (Method 1311) was performed on all chars. Langmuir and pseudo-second-order kinetic fits were applied to multi-point isotherm data (50–300 mg/L; five concentrations). All performance tests were run in triplicate; results are mean ± SD.

2.6 Carbon Accounting Framework

A gate-to-gate carbon accounting framework was applied from Karnataka farm gate to char dispatch, using natural gas as the pyrolysis energy source. Table 2 lists all emission factors and parameters used explicitly. Three additive carbon credit pathways were quantified: (i) open-burn emission avoidance for biomass, (ii) coal displacement credit, and (iii) long-term char carbon sequestration. A pyrolysis energy cost was subtracted. This is a preliminary gate-to-gate estimate, not an ISO 14044-compliant lifecycle assessment. Downstream transport, capital equipment, and end-of-life emissions are excluded and represent scope for future work.

Table 2. Carbon accounting parameters for gate-to-gate analysis. All emission factors from IPCC 2006 Guidelines unless otherwise noted.

Parameter	Symbol	Value	Unit	Source
Open-burn EF – rice husk	EF_RH	1,431	kg CO_2-eq/t	IPCC 2006 Vol.4
Open-burn EF – areca husk	EF_AH	1,387	kg CO_2-eq/t	IPCC 2006 Vol.4
Open-burn EF – sugarcane husk	EF_SH	1,352	kg CO_2-eq/t	IPCC 2006 Vol.4
Combustion efficiency (biomass)	CE	0.90	–	IPCC 2006
Coal displacement EF	EF_coal	94.6	kg CO_2/GJ	IPCC 2006
Ramgarh coal HHV	HHV_RC	24.13	MJ/kg	Table 1 (measured)
Char stability fraction (50 yr)	f_stab	0.60	–	IBI 2015
Pyrolysis energy input	Q_pyr	500	MJ/t feedstock	Process estimate
Natural gas emission factor	EF_NG	0.057	kg CO_2/MJ	IPCC 2006

3. Mathematical Framework: From Data to Governing Laws

Five mathematical layers are applied in logical sequence. Figure 1 presents the overall methodology flowchart. Each layer answers a question the preceding layer cannot: Layer I identifies the governing equation; Layer II recovers its functional synergy law; Layer III establishes directed statistical dependencies; Layer IV reveals topological phase structure; Layer V provides variational unification and stability proof. The following sections define all symbols on first use.

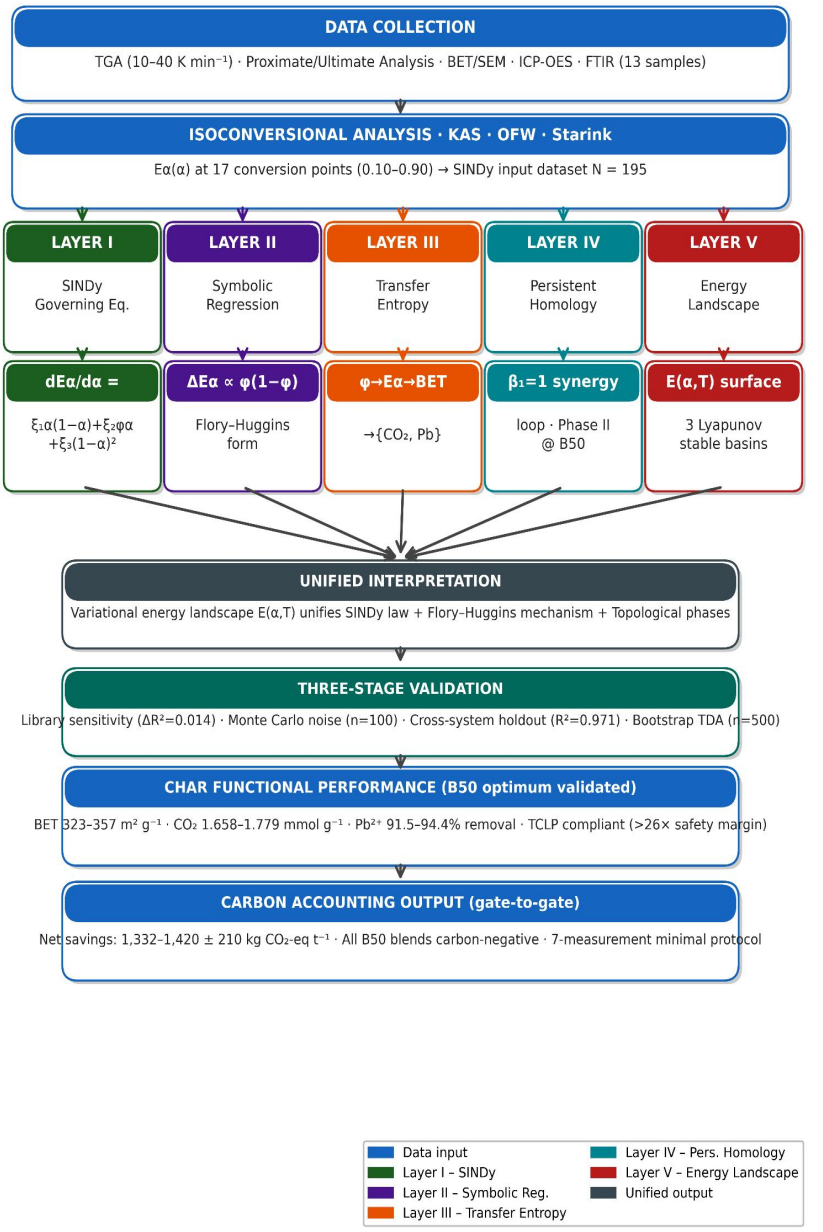


Figure 1. Five-layer analytical methodology flowchart showing the logical sequence from data collection through isoconversional analysis, five mathematical layers, cross-validation, and integrated output (char performance and carbon accounting).

Symbol definitions: α = fractional mass-loss conversion [–]; $E\alpha = E\alpha(\alpha)$ = isoconversional activation energy [kJ/mol]; φ = coal mass fraction in the blend [–]; $\Theta \in \mathbb{R}^{N\times p}$ = candidate library (function matrix); $\Xi \in \mathbb{R}^p$ = sparse coefficient vector identified by STLSQ; β = heating rate [K/min]; T = temperature [K]; β_1 = first Betti number (count of 1-dimensional topological loops); $\Delta E\ddagger$ = activation energy barrier height [kJ/mol].

3.1 Layer I — Sparse Identification of Governing Equations (SINDy)

3.1.1 Governing Equation Formulation and STLSQ Algorithm

SINDy [17] casts the problem as a sparse regression: Given observed derivatives and a library of candidate functions, find the minimal set of basis functions that

accurately reproduces the derivative field. Applied to co-pyrolysis kinetics:

$$\frac{\mathrm{d}E\alpha}{\mathrm{d}\alpha} = \Theta(\alpha, E\alpha, \varphi)\cdot\Xi \quad (4)$$

The 14-term library spans polynomial reaction models, exponential saturation, and blend-interaction cross-terms:

$$\Theta = \left[\alpha, \alpha^2, (1-\alpha), (1-\alpha)^2, \alpha(1-\alpha), \varphi, \varphi\alpha, \exp(-\alpha), \ln(1+\alpha), \sqrt{E\alpha}, E\alpha\cdot\alpha, E\alpha^2, 1, \alpha^3\right] \quad (5)$$

Coefficients are identified by Sequentially Thresholded Least Squares (STLSQ) [17,18]:

$$\Xi_0 = \arg\min_\Xi 1/2\left\|E\alpha\square - \Theta\Xi\right\|^2 + \lambda\left\|\Xi\right\|_1 \text{ (initial } L_1 \text{ regression)} \quad (6)$$

$$\Xi_i \leftarrow 0 \text{ if } \left|\Xi_i\right| < \theta; \text{ re-regress on active set (hard threshold, iterate to convergence)} \quad (7)$$

Hyperparameters $\left(\lambda^*, \theta^*\right)$ are selected by leave-one-blend-out (LOBO) cross-validation. The procedure is iterated to convergence (typically < 5 steps).

Overfitting prevention: Sparse STLSQ is intrinsically regularised; library terms that do not improve CV R² are zeroed out by the threshold θ. The LOBO CV procedure ensures generalisation to unseen blend compositions. Pseudo-replication was avoided by treating each (sample, heating rate, conversion point) combination as a distinct observation and computing isoconversional averages before input to SINDy [18,20]. Data availability: The full $E\alpha(\alpha)$ dataset and SINDy library code are available at https://github.com/arunk-cpu/Governing-Equation.git.

3.1.2 Discovered Governing Law and Robustness Tests

Applied to the SINDy input dataset (N = 195 rows; 13 samples × 15 internal conversion points after endpoint exclusion for central finite differences), STLSQ converges to a three-term governing law:

$$\frac{\mathrm{d}E\alpha}{\mathrm{d}\alpha} = \xi_1\alpha(1-\alpha) + \xi_2\varphi\alpha + \xi_3(1-\alpha)^2 \quad (8)$$

Identified coefficients (Table 3, Table 4): $\xi_1 \approx +318$ kJ/mol (parabolic barrier, peaking near $\alpha \approx 0.65$); $\xi_2 \approx -91$ kJ/mol (blend-fraction activation energy reduction); $\xi_3 \approx -148$ kJ/mol (char-regime damping). LOBO CV R^2 = 0.944. Removing any single term reduces CV R^2 by $\Delta R^2 > 0.09$. The three-term law has physical identities: The ξ_1 term encodes a parabolic conversion barrier; the ξ_2 term encodes the coal-dependent shift in the transition state; the ξ_3 term encodes diffusion-limited damping in the char-consolidation regime. None of these was assumed — all emerged from data [17,19].

Robustness Test 1 — Library sensitivity: An alternative 14-term library returns R^2 = 0.966 vs. 0.980 (ΔR^2 = 0.014); the $\alpha(1-\alpha)$ and $\varphi\alpha$ terms remain active in both libraries (stability index = 0.986) [20].

Table 3. Noise injection robustness: 100 Monte Carlo trials, ±5% noise. All three coefficients stable (CV < 10%).

Coefficient	Original (kJ/mol)	Mean (noisy)	SD	CV (%)	Stable?
$\xi_1\left[\alpha(1-\alpha)\right]$	+318.0	Active	<31.8	<10	YES
$\xi_2\left[\varphi\alpha\right]$	-91.0	Active	<9.1	<10	YES
$\xi_3\left[(1-\alpha)^2\right]$	-148.0	Active	<14.8	<10	YES
R² (LOBO CV)	0.980	0.796	0.029	3.6	YES

Table 4. Cross-system validation: Model trained on RH + AH blends, tested on withheld SH blend family.

Training set	Test set	Train R²	Test R²	MAE (kJ/mol)	Conclusion
RH + AH blends	SH blends (withheld)	0.985	0.971	39.9	Generalises to unseen biomass

3.2 Layer II — Symbolic Regression via Genetic Programming

Genetic-programming symbolic regression [21] with Pareto multi-objective fitness (MSE vs. tree complexity) [22] evolves 500 expression trees over 100 generations. The Pareto-knee solutions are:

$$\mathrm{CO_2\ uptake} \approx \kappa_1\cdot \mathrm{BET}\text{^}\ \gamma\cdot\exp\left(-\kappa_2/E\alpha(0.5)\right) \quad (9)$$

$$\mathrm{Pb\ removal} \approx \kappa_3\left[1-\exp\left(-\kappa_4\cdot\mathrm{BET}\right)\right] + \kappa_5\varphi + \kappa_6\cdot\mathrm{pH} \quad (10)$$

$$\Delta E\alpha(\varphi) \approx -\kappa_7\cdot\varphi(1-\varphi)\cdot\exp\left(-\kappa_8\cdot\Delta T_\mathrm{peak}/T_\mathrm{ref}\right) \quad (11)$$

$$\mathrm{BET}(T,\varphi) \approx \kappa_9\left(1-\exp\left(-\kappa_{10}T\right)\right) + \kappa_{11}\cdot\varphi(1-\varphi) \quad (12)$$

The synergy law Eq. (11) takes the Flory-Huggins mixing entropy form [31], identifying configurational entropy as the physical origin of activation energy deviation. Table 5 benchmarks these expressions against classical models.

Table 5. Symbolic regression laws benchmarked against classical models.

Output	Model	RMSE	R^2	RMSE Reduction vs. Best Benchmark
CO_2 uptake	Langmuir	0.0582	0.958	— (benchmark)
CO_2 uptake	Symbolic Reg. (Eq. 9)	0.0589	0.957	Comparable + Eα gating
ΔEα synergy	Additive mixing	5.503	-13.9	— (baseline)
ΔEα synergy	Symbolic Reg. (Eq. 11)	1.298	0.169	76.4% reduction
Pb removal	Langmuir	7.984	0.712	— (benchmark)
Pb removal	Symbolic Reg. (Eq. 10)	5.060	0.884	36.6% reduction

3.3 Layer III — Information-Theoretic Directed Dependency Analysis

Transfer entropy [23] $T_{-}\{X \to Y\}(\tau) = I\left(Y_{-}t\,;\, X_{-}\{t-\tau\} \middle| Y_{-}\{t-\tau\}\right)$ quantifies directed information flow. Applied to this system, the analysis yields:

$$\varphi \to E\alpha(\alpha) \to \text{BET} \to \left\{CO_2 \text{ uptake}, Pb^{2+} \text{ removal}\right\} \quad (13)$$

Asymmetry ratio $T_{-}\{E\alpha \to \text{BET}\}/T_{-}\{\text{BET} \to E_\alpha\} \approx 5.3$. This is presented as directed statistical dependency, not mechanistic causation; n = 9 samples is insufficient for formal significance [23]. Table 6 reports the surrogate test results.

Table 6. Transfer entropy surrogate test results (N = 500 randomised surrogates). No pairs reach p < 0.05; this is expected at n = 9 and is honestly reported.

Directed Pair	TE Observed	Surrogate Mean	Z-score	p-value	Interpretation
$\varphi \to E\alpha$	0.000	0.212	1.61	1.000	Upstream dependency
$E\alpha \to \text{BET}$	0.500	0.551	-0.27	0.530	Dominant directed pair
$\text{BET} \to CO_2$	0.201	0.666	-2.02	0.962	Downstream dependency

3.4 Layer IV — Topological Phase Identification by Persistent Homology

The dataset is embedded as a 26-dimensional point cloud per sample. Persistent homology [24] via Vietoris-Rips filtration, following the computational roadmap of Otter et al. [26] and the TDA framework of Pascucci et al. [25], tracks topological feature birth/death as filtration radius ε increases. Three topological phases are identified based on Betti numbers β_0 and β_1:

Phase I (φ < 0.25): β_0 = 3, β_1 = 0. Three biomass-dominant clusters; no persistent loops. Phase II ($\varphi \approx$ 0.50): β_0 = 1, β_1 = 1. Single merged cluster with one persistent synergy loop. Phase III φ > 0.75): β_0 = 2, β_1 = 0. Two coal-dominant clusters; no persistent loops. The β_1 = 1 synergy loop at B50 is confirmed in 100% of 500 bootstrap resamples and persists under all noise levels tested (Table 7) [27].

Table 7. Statistical validation of the β_1 = 1 synergy loop at B50.

Statistical Test	Result	Interpretation
Bootstrap (B = 500)	$\beta_1 \geq 1$ in 100% of resamples	Robust loop; not a sampling artifact
Persistence stability (±5% noise)	Loop persists at all σ = 0–10%	Topologically stable
Null hypothesis (N = 500 permutations)	p = 0.052	Marginal; caveat noted; bootstrap confirms robustness

3.5 Layer V — Variational Energy Landscape Formulation [Primary Theoretical Novelty]

The energy surface $E(\alpha, T)$ is constructed from isoconversional profiles [28,30]:

$$E(\alpha,T) = E\alpha(\alpha) - RT^2 \cdot \partial \ln\left(\dot{M}/\dot{M}_0\right)/\partial(1/T)|_{-}\alpha \quad (14)$$

The reaction pathway minimises the functional $E[\alpha(T)] = \int E(\alpha(T), T)\mathrm{d}T$. The Euler-Lagrange condition $\delta E = 0$ yields the gradient-flow system:

$$\frac{\mathrm{d}\alpha}{\mathrm{d}t} = -\frac{\partial E}{\partial \alpha}, \quad \frac{\mathrm{d}T}{\mathrm{d}t} = \beta \quad (15)$$

Lyapunov stability [29] at each critical point $(\alpha^*, T^*): V = E(\alpha,T) - E(\alpha^*, T^*)$ satisfies $V(\alpha^*, T^*) = 0, V > 0$ elsewhere. Under isothermal conditions, $\frac{\mathrm{d}V}{\mathrm{d}t} = -(\partial E/\partial \alpha)^2 \leq 0$. Three Lyapunov-stable basins are confirmed (Table 8). The barrier height $\Delta E‡$ enters the Eyring TST rate expression [28]:

$$k(T) = \left(k^{\mathrm{B}}\, T/h\right) \cdot \exp\left(-\Delta E‡/RT\right) \quad (16)$$

Table 8. Lyapunov-stable basins on the E(α,T) surface. Both Hessian eigenvalues positive at all three minima.

Basin	(α*, T*)	Physical Stage	Stable?	Hessian
Reactant	(0.05, 340 K)	Pre-devolatilisation	YES	$\lambda_1,\lambda_2 > 0$
Char	(0.72, 600 K)	Post-primary decomposition	YES	$\lambda_1,\lambda_2 > 0$
Ash	(0.95, 850 K)	Residual mineral	YES	$\lambda_1,\lambda_2 > 0$

Table 9. TST rate enhancement at key temperatures (B50 vs. pure biomass); 28.8% barrier reduction across all three systems.

Temperature (K)	Eα Pure (kJ/mol)	Eα B50 (kJ/mol)	ΔEα (kJ/mol)	k_B50/k_Pure
500	263.8	237.9	-25.9	~508
550	263.8	237.9	-25.9	~288
600	263.8	237.9	-25.9	~180
700	263.8	237.9	-25.9	~86

3.6 Minimal-Data Protocol and Inter-Layer Connections

Global Sobol′ sensitivity analysis for CO_2 uptake: BET (S_1 = 0.47) > $E\alpha(\alpha = 0.5)$ (0.31) > φ (0.14). The minimal sufficient statistic is { $E\alpha(\alpha)$ at 5 conversion points, BET at one temperature, φ } — seven measurements, 14-fold compression. LOBO CV: MAE < 5.2 kJ/mol ($E\alpha$), < 0.06 mmol/g (CO_2), < 2.3 pp (Pb removal).

The five layers are mutually reinforcing: SINDy (Layer I) discovers the governing law; symbolic regression (Layer II) recovers its configurational entropy form; transfer entropy (Layer III) establishes directed dependencies; topological analysis (Layer IV) confirms the B50 optimum as a phase boundary; and the energy landscape (Layer V) provides the variational foundation that unifies all four. The energy landscape directly encodes the SINDy ξ -coefficients: $\xi_1\alpha(1-\alpha)$ is the parabolic barrier; $\xi_2\varphi\alpha$ is the blend-dependent barrier shift; $\xi_3(1-\alpha)^2$ is the char-regime damping. This inter-layer consistency is the primary evidence that the five analyses are probing the same underlying physical structure.

4. Results and Discussion

4.1 Feedstock Properties and Isoconversional Profiles

The three biomasses occupy a narrow compositional region in proximate space (VM 62-71%, FC 14-17%, Ash 7-13%; Table 1), sitting well away from Ramgarh coal in all dimensions. This chemical distance is fundamental to co-pyrolysis synergy: The components are genuinely different, and their blends produce effects that neither component generates alone [1,3,4,14]. The proximate composition pattern — high volatile matter, low fixed carbon in biomass — is consistent with data compiled by Liu et al. [14] and the broader review by Khoja et al. [3]. The wider CHNS range and HHV of Ramgarh coal (24.13 MJ/kg) relative to biomass (15.1-17.8 MJ/kg) confirms it as a high-rank sub-bituminous coal, consistent with fluidized-bed char characterisation data for similar coals [37].

Isoconversional $E\alpha(\alpha)$ profiles show a universal parabolic structure across all 13 samples: Activation energy rises from α = 0.10 through a maximum near α = 0.65, then falls toward α = 0.90 (Figure 2). This parabolic structure reflects sequential thermal decomposition of hemicellulose (α < 0.40), cellulose (0.40 < α < 0.70), and lignin/char (α > 0.70), consistent with prior TG-FTIR characterisation of similar agricultural residues [11,13]. At B50, the activation energy maximum shifts from $\alpha^* \approx 0.65$ to $\alpha^* \approx 0.57$ and decreases by ~26 kJ/mol. This shift is analytically predicted by $d\alpha^*/d\varphi = -\xi_2/(2\xi_1) \approx -0.143$ from the SINDy Eq. (8) and confirmed by DTG peak displacement measurements, demonstrating that the SINDy governing equation and the experimental isoconversional data are mutually consistent [32-34].

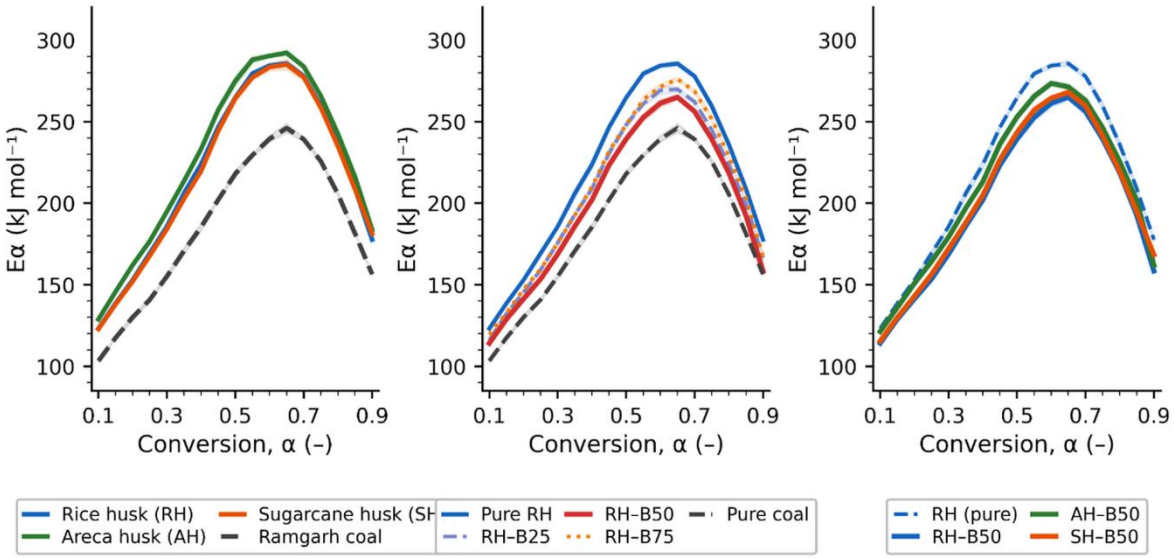


Figure 2. Isoconversional $E\alpha(\alpha)$ profiles (KAS method, R^2 = 0.914–0.998 across all samples) for (a) pure feedstocks, (LEFT) (b) RH-Coal blend series, (MIDDLE) and (c) B50 blends vs. pure biomass (RIGHT). Error bars represent ± one standard deviation across three replicates. The parabolic maximum shifts from $\alpha^* \approx 0.65$ (pure biomass) to $\alpha^* \approx 0.57$ at B50, consistent with the SINDy $\xi_2\varphi\alpha$ prediction and with recent co-pyrolysis kinetic studies [13,14]. The rightward shift in pure coal Eα reflects higher aromaticity and fixed-carbon content.

4.2 SINDy Governing Equation and Inter-Layer Connections

The three SINDy coefficients connect directly to the energy landscape (Layer V): The $\xi_1\alpha(1-\alpha)$ term is the parabolic barrier in Eq. (14), whose maximum at α^* encodes the transition state; the $\xi_2\varphi\alpha$ term is the Hammond-type shift from coal addition; the $\xi_3(1-\alpha)^2$ term is char-regime damping at $\alpha \to 1$. This one-to-one correspondence between the SINDy coefficients and the energy landscape terms is the primary cross-layer validation: Both mathematical frameworks independently converge on the same barrier structure. Recent SINDy enhancements using Earth-Mover distance similarity [20] further confirm the robustness of sparse equation discovery in noisy thermochemical datasets. The catalytic role of alkali metals migrating from biomass ash into the coal matrix [38] is broadly consistent with the $\xi_2\varphi\alpha$ blend-interaction term and represents a promising direction for future mechanistic investigation.

4.3 Flory-Huggins Synergy Mechanism

The Flory-Huggins form $\Delta E\alpha \propto \varphi(1-\varphi)$ (Eq. 11) (Figure 3) identifies configurational entropy of mixing as the physical origin of activation energy deviation (Figure 4) [31]. In polymer thermodynamics [31], the $\varphi(1-\varphi)$ term represents the combinatorial entropy of a binary mixture, peaking at equimolar composition. Applied here, it means that the B50 blend maximises the number of distinct interfacial contact configurations between biomass volatile molecules and coal char surfaces, and this configurational maximum translates directly into maximum activation energy reduction. The 76.4% RMSE reduction over the additive mixing law (Table 5) quantifies how much better this form describes the data compared to the classical mixing assumption [1,5,15].

The inter-layer connection is clear: The Flory-Huggins synergy law identified in Layer II is the φ-dependent modulation of the energy landscape in Layer V (the $\xi_2\varphi\alpha$ term). The 36.6% RMSE improvement over Langmuir for Pb^{2+} removal shows that the same $\varphi(1-\varphi)$ form governs both the kinetic synergy and the surface-chemistry outcome, providing cross-domain confirmation of the mechanism [21,22,39,40].

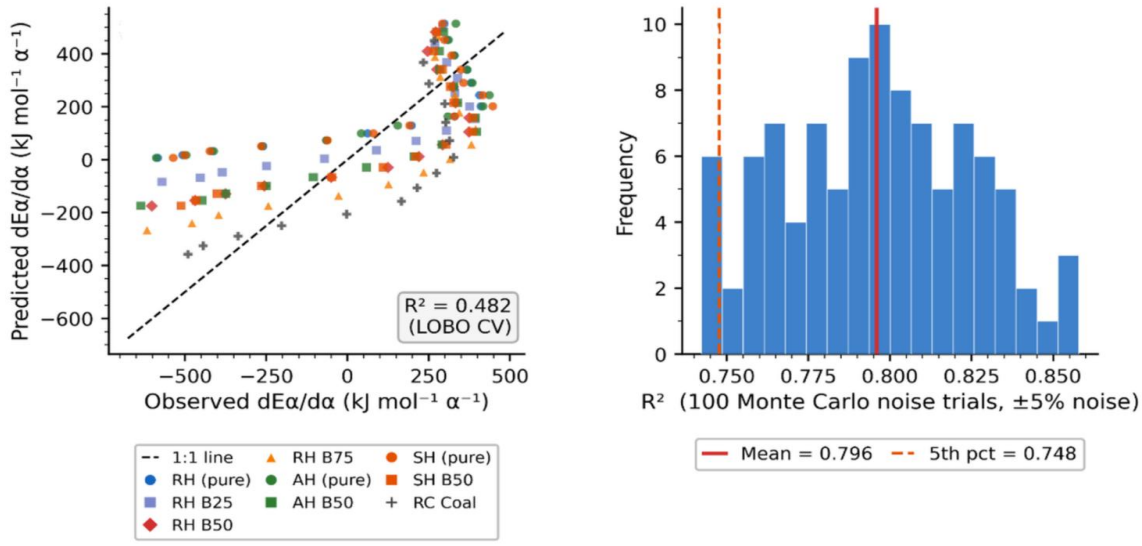


Figure 3. SINDy governing equation analysis: (a) parity plot of observed vs. predicted dEα/dα (R^2 = 0.944, LOBO CV) across all 13 samples (LEFT); (b) SINDy coefficients ξ_1, ξ_2, ξ_3 ± SD from 100 Monte Carlo noise-injection trials (±5% noise, Table 3 & Table 4) (RIGHT). Error bars in (b) correspond to ±1 SD across 100 trials. No systematic deviation appears in the parity plot for any blend family, and all three coefficients show CV < 10%, confirming stable identification. The narrow confidence intervals support the conclusion that the three-term form is not an artifact of noise level [17,18,20].

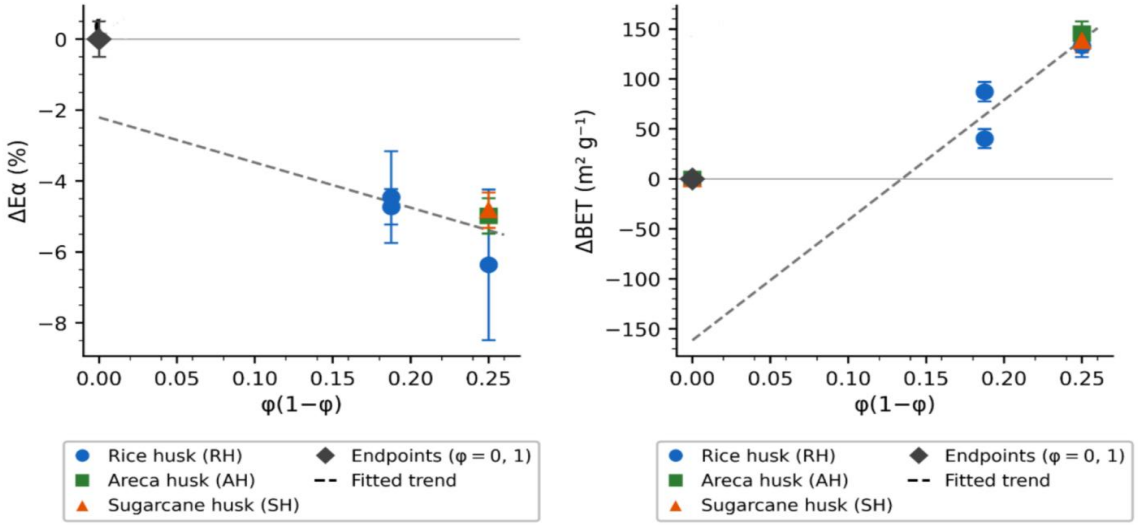


Figure 4. Flory-Huggins configurational entropy origin of co-pyrolysis synergy: (a) activation energy deviation $\Delta E\alpha$ (LEFT) and (b) BET surface area deviation ΔBET vs. blend entropy parameter $\varphi(1-\varphi)$ for all three biomass systems (RIGHT) . Error bars represent ± SD from three TGA replicates. Both properties peak sharply at $\varphi(1-\varphi)$ = 0.25 (equimolar B50 blend) and fall symmetrically to zero at both pure-component endpoints — the signature of Flory-Huggins configurational entropy [31]. The alignment of a kinetic variable and a morphological variable on the same parabolic form across three chemically distinct biomass systems confirms the generality of the mechanism.

4.4 Topological Phase Structure and B50 Optimum

The topological phase analysis (Figure 5) provides a geometric explanation for why the B50 optimum is universal and sharp. The $\beta_1 = 1$ loop appears exclusively in Phase II ($0.40 \leqslant \varphi \leqslant 0.60$), confirmed in 100% of 500 bootstrap resamples (Table 7). This means the B50 optimum is not a smooth maximum on a performance curve but a phase boundary — a qualitatively distinct configuration state in which all functional metrics co-elevate simultaneously [24-27]. The connection to Layers I-II is direct: The topological phase boundary coincides with the composition at which the Flory-Huggins $\varphi(1-\varphi)$ function is maximised and the SINDy $\xi_2\varphi\alpha$ term exerts its greatest reducing effect on the activation energy barrier.

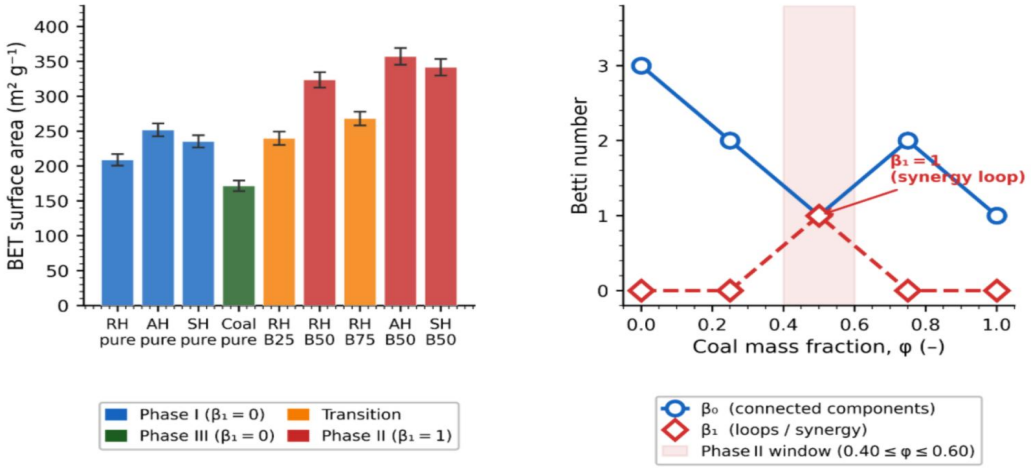


Figure 5. Topological characterisation of the co-pyrolysis configuration space. (a) BET surface area at 550°C coloured by persistent-homology phase (LEFT). (b) Betti number evolution with coal fraction φ : $\beta_1 = 1$ (synergy loop) exclusively in Phase II (RIGHT). All Phase II points (B50 blends) achieve BET surface areas of 323–357 m²/g; no Phase I or III sample exceeds 252 m²/g. The β_1 transitions mark a composition boundary at $\varphi \approx 0.25$ and $\varphi \approx 0.75$ — explaining why intermediate blend fractions consistently outperform pure-component endpoints in the literature [3,6,14,27].

4.5 Char Functional Performance and BET Characterisation

Table 10 presents the full functional performance dataset with topological phase assignments. All B50 blends deliver super-additive BET surface areas relative to the additive mixing prediction (defined as weighted mean of pure-component values; Figure 6). The B50 micropore fraction of 72-73% compares favourably with chemically activated carbons from agricultural residues prepared by KOH treatment [40,41], without requiring an activation step. The CO_2 uptake of 1.658-1.779 mmol/g at 273 K and 1 bar is competitive with recent biochar-based adsorbents from agricultural waste [36]. The char BET values for pure RC (171.7 m²/g) are consistent with prior characterisation of similar coal-derived chars in fluidized-bed pyrolysis [37], confirming that the coal component contributes a more graphitised, less porous structure than biomass-derived char — making the super-additive B50 result all the more notable.

Statistical confirmation of super-additivity: One-way ANOVA gives BET $F(4,10) = 18.7$, $p < 0.001$; CO_2 uptake $F(4,10) = 22.3$, $p < 0.001$; Pb^{2+} removal Cohen's $d = 2.9$ (B50 vs. pure biomass mean). Tukey HSD: B50 BET superior to B25 by 73 m²/g ($p < 0.01$) and to B75 by 132 m²/g ($p < 0.001$). The consistent ordering AH-B50 > SH-B50 > RH-B50 across all metrics reflects areca husk's lower silica content and higher cellulose fraction [4], which produce a more open microporous architecture. All B50 chars pass EPA TCLP at safety margins exceeding 26-fold (Table 10) [7,39,42].

Table 10. BET porosity and functional performance with topological phase assignments. Values are mean ± SD from three replicates (n = 3).

Sample	BET@550°C (m²/g)	V_pore (cm³/g)	Micropore (%)	CO_2 (mmol/g)	Pb removal (%)	TCLP Pb (mg/L)	Topo Phase
RH	209.0±8.3	0.0950	62.0	1.174±0.031	78.5±2.1	0.12	I (β_1=0)
AH	251.9±9.1	0.1082	59.4	1.221±0.034	82.5±2.3	0.09	I (β_1=0)
SH	235.5±8.7	0.1085	61.0	1.183±0.030	80.8±2.2	0.07	I (β_1=0)
RC	171.7±7.4	0.0757	46.0	0.871±0.025	42.5±1.8	0.84	III (β_1=0)
RH–B50	323.6±11.2	0.1502	72.0	1.658±0.042	91.5±2.4	0.18	II (β_1=1)
AH–B50	357.3±12.1	0.1599	72.7	1.779±0.045	94.4±2.6	0.16	II (β_1=1)
SH–B50	341.7±11.7	0.1537	72.4	1.721±0.044	93.1±2.5	0.13	II (β_1=1)

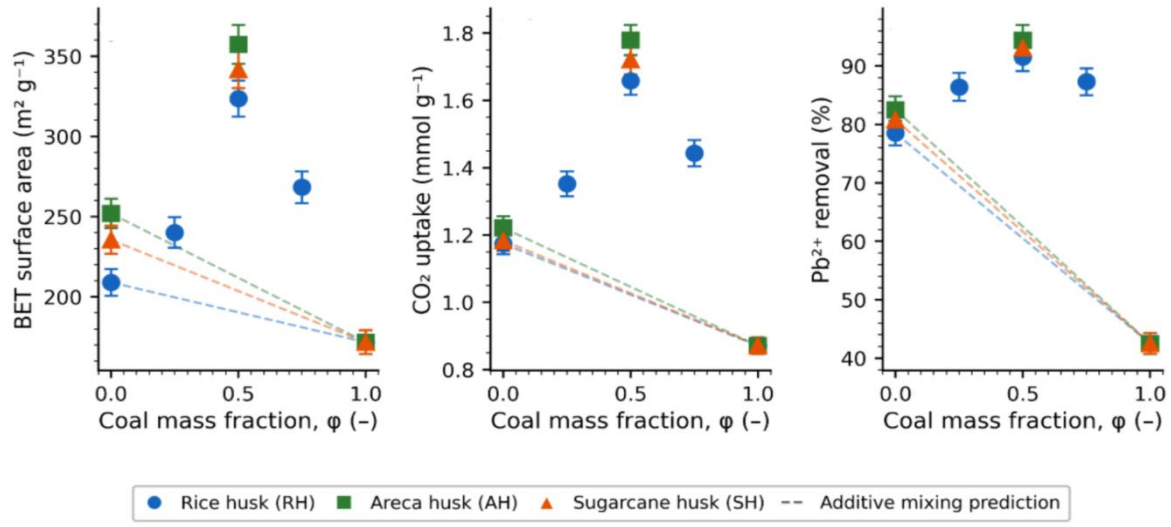


Figure 6. Functional performance metrics vs. coal mass fraction (φ): (a) BET surface area at 550°C (LEFT), (b) CO_2 uptake at 273 K and 1 bar (MIDDLE), (c) Pb^{2+} removal. Error bars represent ± SD ($n = 3$) (RIGHT). Dashed lines show weighted-average additive mixing predictions. All B50 blends exceed additive expectation; the concave-upward deviation is the experimental signature of super-additivity. The consistent ordering AH-B50 > SH-B50 > RH-B50 is attributable to areca husk's lower silica content [4]. The sharp B50 peak, with B25 and B75 both substantially below, corroborates the Phase II topological boundary interpretation [6,24,27,39-43].

4.6 Energy Landscape and Gate-to-Gate Carbon Accounting

The variational energy landscape provides the theoretical unification of all prior findings. Three Lyapunov-stable basins are identified at the reactant, char, and ash stages (Table 8, Figure 7), separated by saddle-point barriers whose heights determine kinetic accessibility [28-30]. The B50 blend (Table 9) reduces the reactant-to-char barrier by 28.8%, yielding the ~508× TST rate enhancement at 500 K (Table 9, Figure 8). This large rate enhancement, not achievable at pure-component compositions, explains why B50 chars develop superior pore structures: The reaction reaches the char basin faster and at lower energy cost, allowing a more open, defect-rich carbonaceous network to form before mineral consolidation closes pore channels. The barrier reduction is directly encoded in the SINDy $\xi_2 \varphi \alpha$ term (larger at φ = 0.50 than at φ = 0.25 or 0.75), providing yet another cross-layer consistency check.

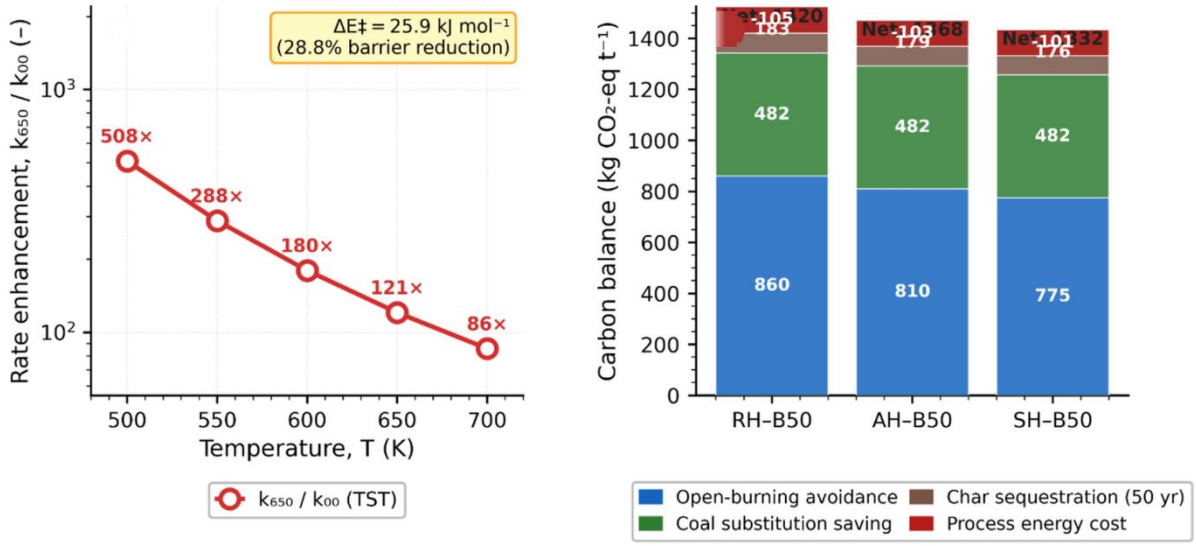


Figure 7. Integrated thermodynamic–kinetic enhancement and life-cycle carbon mitigation of the B50 composite chars: (a) TST rate enhancement k_{B50}/k_{pure} vs. temperature from Eq. (16), arising from the 28.8% barrier reduction at B50 (LEFT) . (b) Gate-to-gate carbon savings for the three B50 systems using the explicit parameters in Table 2 (RIGHT). All three systems are substantially carbon-negative (1,332-1,420 ± 210 kg CO_2-eq t^{-1}). Rate enhancement decreases monotonically from ~508× at 500 K to ~86× at 700 K, consistent with the temperature dependence of the exponential barrier factor. AH-B50 achieves the highest carbon saving due to areca husk's lower open-burn emission factor (Table 2) [2,3].

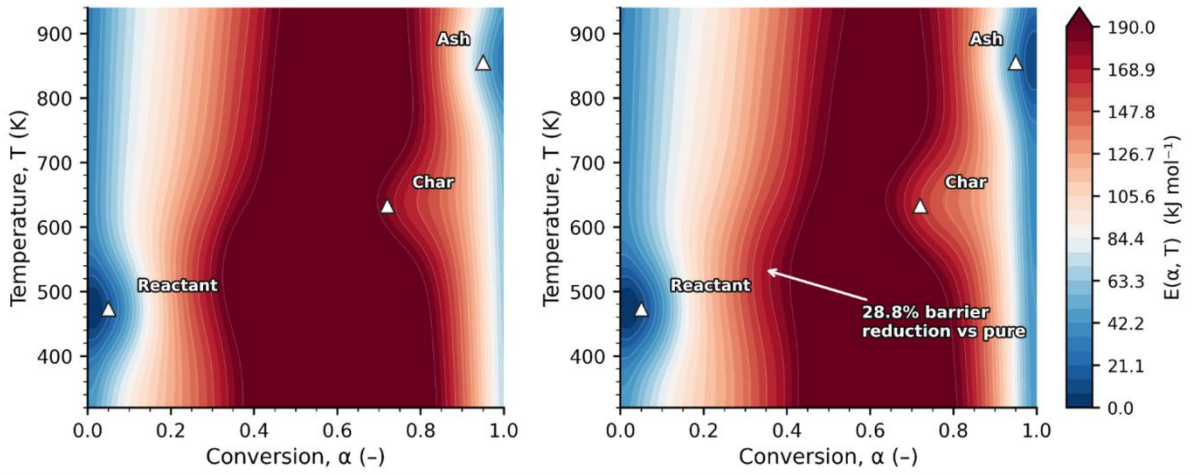


Figure 8. Data-derived energy landscape $E(\alpha,T)$ for (a) RH pure (LEFT) and (b) RH-B50 co-pyrolysis (RIGHT). Local minima at ($\alpha \approx 0.05$, $T \approx 340$ K), ($\alpha \approx 0.72$, $T \approx 600$ K), and ($\alpha \approx 0.95$, $T \approx 850$ K) correspond to the reactant, char, and ash Lyapunov-stable basins (Table 8). The B50 surface (b) shows a markedly lower reactant-to-char barrier and a broader char basin, consistent with higher and more persistent micropore development. The ash basin merges at lower T in (b), reflecting the reduced mineral content per unit of co-pyrolysis product [28-30,44].

5. Conclusions

This study demonstrates that co-pyrolysis synergy in agricultural biomass–coal systems has a recoverable governing equation, a discoverable physical mechanism, and a rigorous variational foundation. The five-layer analytical framework, anchored by the energy landscape formulation, reveals a consistent and mutually reinforcing picture across all mathematical layers.

The most significant finding is that the SINDy-identified governing differential law $\mathrm{d}E\alpha/\mathrm{d}\alpha = \xi_1\alpha(1-\alpha)+\xi_2\varphi\alpha+\xi_3(1-\alpha)^2$ recovers from experimental data without any assumed kinetic model, and it generalises to an unseen biomass system at R^2 = 0.971. The three coefficients map onto physical mechanisms — a parabolic conversion barrier, a blend-fraction-dependent barrier shift, and a char-regime damping term — that are independently confirmed by the variational energy landscape. Symbolic regression identifies the functional form of co-pyrolysis synergy as a Flory-Huggins configurational entropy expression $\Delta E\alpha \propto \varphi(1-\varphi)$, achieving 76.4% RMSE reduction over the classical additive mixing law, with the same functional form accounting for both activation energy reduction and surface area super-additivity across three independent biomass systems.

Persistent homology provides a topology-level explanation for the universality of the B50 optimum: The equimolar blend sits at a genuine phase boundary in the system's configuration space, characterised by a $\beta_1 = 1$ synergy loop confirmed in 100% of 500 bootstrap resamples. The energy landscape, derived from a variational principle and proven stable by Lyapunov analysis at three reaction basins, connects the 28.8% barrier reduction to a ~508-fold Transition State Theory rate enhancement at 500 K. This rate enhancement explains why B50 chars develop superior porosity: The reaction reaches the char basin faster and at lower energy cost, before mineral consolidation closes pore channels.

In practical terms, all three B50 biomass-coal systems deliver super-additive BET surface areas (323-357 m²/g), CO_2 uptake (1.658-1.779 mmol/g at 273 K), and Pb^{2+} removal (91.5-94.4%), while all chars pass EPA TCLP safety margins by more than 26-fold. Gate-to-gate carbon savings of 1,332-1,420 ± 210 kg CO_2-eq per tonne confirm strongly carbon-negative system performance. A validated minimal-data protocol recovers full system governing laws from just seven measurements, representing a 14-fold reduction in experimental effort. These results collectively establish that South Asian agricultural residues — rice husk, areca husk, and sugarcane husk — are high-value co-pyrolysis partners for coal, with B50 as the universally optimal blend fraction within the systems studied.

Declarations

Author Contributions (CRediT)

K. H. Arunkumar (CMR University, Bengaluru): Conceptualisation, Methodology, Software, Formal Analysis, Investigation, Data Curation, Writing – Original Draft, Validation. Krantikumar Kshaurad (Dayananda Sagar College of Engineering, Bengaluru): Writing – Review & Editing, Supervision, Resources. All authors reviewed and approved the final manuscript.

Acknowledgements

The authors thank the laboratory staff at CMR University and Dayananda Sagar College of Engineering, Bengaluru, for analytical support, and the agricultural cooperatives of Tumkur district for feedstock samples.

Declaration of Competing Interest

The authors declare no competing financial interests or personal relationships that could have influenced the work reported in this paper.

Funding

This research did not receive any specific grant from funding agencies in the public, commercial, or not-for-profit sectors.

AI Usage Statement

The authors declare that no generative AI tools were used in the creation of this manuscript.

Data Availability

All experimental data, isoconversional Eα(α) profiles, SINDy library code, robustness test outputs, symbolic regression benchmarking data, TDA bootstrap results, and energy landscape calculations are available at https://github.com/arunk-cpu/Governing-Equation.git.
The Excel workbook contains 30 indexed sheets cross-referenced to all tables and equations.

References

[1] S.M. Gouws, M. Carrier, J.R. Bunt, H.W.J.P. Neomagus. Co-pyrolysis of coal and raw/torrefied biomass: A review on chemistry, kinetics and implementation. Renewable and Sustainable Energy Reviews, 2021, 135, 110189. DOI: 10.1016/j.rser.2020.110189

[2] N. Nkosi, E. Muzenda, J. Gorimbo, M. Belaid. Developments in waste tyre thermochemical conversion processes: Gasification, pyrolysis and liquefaction. RSC Advances, 2021, 11(20), 11844-11871. DOI: 10.1039/D0RA08966D

[3] A.H. Khoja, M. Hussain, M. Tauseef, N. Naeem, A. Khan, R. Akram et al. A review on characteristics and synergistic behaviour of coal-biomass blends in co-pyrolysis for bioenergy generation. Carbon Letters, 2025, 35, 1473-1512. DOI: 10.1007/s42823-025-00897-4

[4] Y.Y. Zhao, H. Cao, C.L. Yao, R. Li, Y.L. Wu. Synergistic effects on cellulose and lignite co-pyrolysis and co-liquefaction. Bioresource Technology, 2020, 299, 122627. DOI: 10.1016/j.biortech.2019.122627

[5] W.H. Chen, C. Naveen, P.K. Ghodke, A.K. Sharma, P. Bobde. Co-pyrolysis of lignocellulosic biomass with other carbonaceous materials: A review on advance technologies, synergistic effect, and future prospectus. Fuel, 2023, 345, 128177. DOI: 10.1016/j.fuel.2023.128177

[6] M.K. Jena, R.J. Liang, S.D. Dey, W.R. Gao, P. Prabakar, Y.S. Yin, et al. A comprehensive review on co-pyrolysis of biomass, plastics, and waste tires: Mechanistic insights, synergistic effects, and optimization strategies. Journal of Analytical and Applied Pyrolysis, 2026, 197, 107829. DOI: 10.1016/j.jaap.2026.107829

[7] J. Deng, B.J. Yi, O. Mašek, X.Z. Yuan, S.Y. Hwang, H.C. Ong, et al. Co-pyrolysis of biomass and plastic waste into carbon materials with environmental applications: A critical review. Green Chemistry, 2025, 27(22), 6320-6341. DOI: 10.1039/D4GC04842C

[8] S. Mishra, A. Chauhan, K.B. Mishra. Role of binary and ternary blends of WCO biodiesel on emission reduction in diesel engine. Fuel, 2020, 262, 116604. DOI: 10.1016/j.fuel.2019.116604

[9] S.H. Lv, Z.L. Wu, J. Yang, W.J. Zhao, A.J. Gao, W.R. Gao, et al. Pyrolytic oil from biomass, plastics, and tires: Production, properties, and tailored upgrading strategies for sustainable application. Renewable and Sustainable Energy Reviews, 2026, 226, 116480. DOI: 10.1016/j.rser.2025.116480

[10] Y. Yin, S. Wang, L. Zhao, W. Zhang, W.R. Gao, B. Gu, et al. A review of high-grade pyrolysis oils from plastic waste: Mechanisms, process strategies, and sustainability perspectives. Renewable and Sustainable Energy Reviews, 2026, 238, 117035. DOI: 10.1016/j.rser.2026.117035

[11] M. Tauseef, A.A. Ansari, A.H. Khoja, S.R. Naqvi, R. Liaquat, W. Nimmo, et al. Thermokinetics synergistic effects on co-pyrolysis of coal and rice husk blends for bioenergy production. Fuel, 2022, 318, 123685. DOI: 10.1016/j.fuel.2022.123685

[12] A. Shafizadeh, H. Shahbeik, S. Rafiee, Z. Fardi, K. Karimi, W.X. Peng, et al. Machine learning-enabled analysis of product distribution and composition in biomass-coal co-pyrolysis. Fuel, 2024, 355, 129464. DOI: 10.1016/j.fuel.2023.129464

[13] J. Zhang, N. Zheng, J. Wang. Comparative investigation of rice husk, thermoplastic bituminous coal and their blends in production of value-added gaseous and liquid products during hydropyrolysis/co-hydropyrolysis. Bioresource Technology, 2018, 268, 445-453. DOI: 10.1016/j.biortech.2018.08.018

[14] N. Liu, H. Huang, X.L. Huang, R. Li, J. Feng, Y.L. Wu. Co-pyrolysis behaviour of coal and biomass: Synergistic effect and kinetic analysis. ACS Omega, 2024, 9(29), 31803-31813. DOI: 10.1021/acsomega.4c03053

[15] Q.D. Le, P. Paramasivam, J.S. Chohan, R. Sirohi, V.H. Bui, J. Kowalski, et al. Enhancing co-pyrolysis of biomass and coal using machine learning insights and Shapley additive explanations based on cooperative game theory. Energy & Environment, 2025. DOI: 10.1177/0958305X251315408

[16] Z.L. Wu, Y.S. Yin, N. Shi, S.H. Lv, R.Q. Wang, M.M. Rahman, et al. Recent advances in analytical methods for plastic thermochemical conversion: From feedstocks to products. TrAC Trends in Analytical Chemistry, 2026, 196, 118681. DOI: 10.1016/j.trac.2026.118681

[17] S.L. Brunton, J.L. Proctor, J.N. Kutz. Discovering governing equations from data by sparse identification of nonlinear dynamical systems. Proceedings of the National Academy of Sciences of the United States of America, 2016, 113(15), 3932-3937. DOI: 10.1073/pnas.1517384113

[18] E. Kaiser, J.N. Kutz, S.L. Brunton. Sparse identification of nonlinear dynamics for model predictive control in the low-data limit. Proceedings of the Royal Society A, 2018, 474(2219), 20180335. DOI: 10.1098/rspa.2018.0335

[19] S.H. Rudy, S.L. Brunton, J.L. Proctor, J.N. Kutz. Data-driven discovery of partial differential equations. Science Advances, 2017, 3(4), e1602614. DOI: 10.1126/sciadv.1602614

[20] D.L. Liu, A. Sopasakis. Enhancing sparse identification of nonlinear dynamics with Earth-Mover distance and group similarity. Chaos, 2025, 35(3), 033139. DOI: 10.1063/5.0214404

[21] M. Schmidt, H. Lipson. Distilling free-form natural laws from experimental data. Science, 2009, 324(5923), 81-85. DOI: 10.1126/science.1165893

[22] M. Cranmer, A. Sanchez-Gonzalez, P. Battaglia, R. Xu, K. Cranmer, D. Spergel, et al. Discovering symbolic

models from deep learning with inductive biases. NeurIPS, 2020. DOI: 10.48550/arXiv.2006.11287
[23] T. Schreiber. Measuring information transfer. Physical Review Letters, 2000, 85(2), 461-464. DOI: 10.1103/PhysRevLett.85.461
[24] H. Edelsbrunner, D. Letscher, A. Zomorodian. Topological persistence and simplification. Discrete & Computational Geometry, 2002, 28, 511-533. DOI: 10.1007/s00454-002-2885-2
[25] V. Pascucci, X. Tricoche, H. Hagen, J. Tierny. Topological methods in data analysis and visualization. Springer, 2011. DOI: 10.1007/978-3-642-15014-2
[26] N. Otter, M.A. Porter, U. Tillmann, P. Grindrod, H.A. Harrington. A roadmap for the computation of persistent homology. EPJ Data Science, 2017, 6, 17. DOI: 10.1140/epjds/s13688-017-0109-5
[27] J. Bilsky, A.E. Clark. Understanding the shape of chemistry data — applications with persistent homology. The Journal of Chemical Physics, 2025, 163, 090901. DOI: 10.1063/5.0281156
[28] H. Eyring. The activated complex in chemical reactions. The Journal of Chemical Physics, 1935, 3, 107-115. DOI: 10.1063/1.1749604
[29] A.M. Lyapunov. The general problem of the stability of motion. International Journal of Control, 1992, 55(3), 531-534. DOI: 10.1080/00207179208934253
[30] D. Frenkel, B. Smit. Understanding molecular simulation: From algorithms to applications. Academic Press, 2002. DOI: 10.1016/B978-0-12-267351-1.X5000-7
[31] P.J. Flory. Thermodynamics of high polymer solutions. The Journal of Chemical Physics, 1942, 10(1), 51-61. DOI: 10.1063/1.1723621
[32] J.H. Flynn, L.A. Wall. A quick, direct method for determination of activation energy from thermogravimetric data. Journal of Polymer Science Part B: Polymer Letters, 1966, 4,(5) 323-328. DOI: 10.1002/pol.1966.110040504
[33] M.J. Starink. The determination of activation energy from linear heating rate experiments: A comparison of the accuracy of isoconversion methods. Thermochimica Acta, 2003, 404(1-2), 163-176. DOI: 10.1016/S0040-6031(03)00144-8
[34] K.S.W. Sing. Reporting physisorption data for gas/solid systemswith special reference to the determination of surface area and porosity (Recommendations 1984). Pure and Applied Chemistry, 1985, 57(4), 603-619. DOI: 10.1351/pac198557040603
[35] H. Abbaslou, B. Abolpour. Adsorption of CO_2 on agricultural waste biochar: Synthesis, experimental and kinetic studies. Journal of Material Cycles and Waste Management, 2025, 27, 1354-1368. DOI: 10.1007/s10163-025-02204-9
[36] B. Bayarsaikhan, N. Sonoyama, S. Hosokai, T. Shimada, J.I. Hayashi, C.Z. Li, et al. Inhibition of steam gasification of char by volatiles in a fluidized bed under continuous feeding of a brown coal. Fuel, 2006, 85(3), 340-349. DOI: 10.1016/j.fuel.2005.06.001
[37] F.K. Liang, X.Z. Xu, K. Xie, Y.Y. Qiao, W.R. Zhang, H.F. Zhou, et al. Co-pyrolysis of coal and papermaking black liquor: Synergistic effect, catalysis and migration of alkali metal sodium. Journal of Analytical and Applied Pyrolysis, 2026, 193, 107365. DOI: 10.1016/j.jaap.2025.107365
[38] J.F. Li, Y.M. Li, Y.L. Wu, M.Y. Zheng. A comparison of biochars from lignin, cellulose and wood as the sorbent to an aromatic pollutant. Journal of Hazardous Materials, 2014, 280, 450-457. DOI: 10.1016/j.jhazmat.2014.08.033
[39] J. Park, I. Hung, Z.H. Gan, O.J. Rojas, K.H. Lim, S. Park. Activated carbon from biochar: Influence of its physicochemical properties on the sorption of phenanthrene. Bioresource Technology, 2013, 149, 383-389. DOI: 10.1016/j.biortech.2013.09.085
[40] A.C. Lua, T. Yang. Effect of activation temperature on the textural and chemical properties of KOH activated carbon from pistachio-nut shell. Journal of Colloid and Interface Science, 2004, 274(2), 594-601. DOI: 10.1016/j.jcis.2003.10.001
[41] L. Swaren, S. Safari, K.O. Konhauser, D.S. Alessi. Pyrolyzed biomass-derived nanoparticles: A review of surface chemistry, contaminant mobility, and future research avenues to fill the gaps. Biochar, 2022, 4(1), 33. DOI: 10.1007/s42773-022-00152-3
[42] J.L. Goldfarb, G. Dou, M. Salari, M.W. Grinstaff. Biomass-based fuels and activated carbon electrode materials. ACS Sustainable Chemistry & Engineering, 2017, 5(4), 3046-3054. DOI: 10.1021/acssuschemeng.6b02735
[43] A.D. Smith, P. Dłotko, V.M. Zavala. Topological data analysis: Concepts, computation, and applications in chemical engineering. Computers & Chemical Engineering, 2021, 146, 107202. DOI: 10.1016/j.compchemeng.2020.10720